IEEE Access
Multidisciplinary ⋮ Rapid Review ⋮ Open Access Journal

Received February 23, 2022, accepted March 5, 2022, date of publication March 16, 2022, date of current version April 7, 2022.

Digital Object Identifier 10.1109/ACCESS.2022.3159693

Fault Diagnosis of HTS–SLIM Based on 3D Finite Element Method and Hilbert–Huang Transform

ALI AHMADPOUR[1], ABDOLMAJID DEJAMKHOOY[1], AND HOSSEIN SHAYEGHI[1,2], (Senior Member, IEEE)
[1]Department of Electrical Engineering, University of Mohaghegh Ardabili, Ardabil 5613793945, Iran
[2]Energy Management Research Center, University of Mohaghegh Ardabili, Ardabil 5613793945, Iran

Corresponding author: Abdolmajid Dejamkhooy (majiddejam@uma.ac.ir)

ABSTRACT The Linear Induction Motors (LIMs) are a novel structure of industrial motors, which have appeared in recent years. There are various models of optimal LIMs that help better performance. However, no research could be found about the behavior of these motors under the fault conditions. In this paper, a High–Temperature Superconducting Single–sided LIM (HTS–SLIM), with flat–solid secondary sheet is considered. Besides, a comprehensive review of novel and robustness fault diagnosis methods in electrical machines is carried out. To satisfy the paper aims, two mechanical and electrical failures, in forms of broken conductor sheet and short–circuit of coil are considered, respectively, and the dynamic model of the studied motor under short–circuit fault is proposed. The motor is modeled with 3D Finite Element Method (FEM), in order to consider the 3D effects of linear motors. Finally, the electromagnetic and mechanical behaviors of the considered machine are rendered under various conditions. The variation of various parameters are studied and their increament or decreament under faulty states are analyzed. In the next step, the Hilbert–Huang Transform (HHT) is employed to detect the features of the mentioned faults. The results and analysis show that the thrust and speed of motor have decreased under short circuit faults, and they have increased suddenly, when the primary cross over the broken secondary sheet about 600 % and 43 %, respectively. Besides, the flux density of all components under short circuit is reduced, while it increased under broken sheet fault and when these faults occur simultaneously.

INDEX TERMS Fault diagnosis, finite element method, high–temperature superconducting, Hilbert–Huang transform, linear induction motor.

I. INTRODUCTION

A. MOTIVATION

Linear Induction Motors (LIMs) are the most powerful candidate for transmission or traction applications due to these motors benefits such as low-cost, no fraction, simple construction and high speed. However, like as other rotary electrical machines, the linear machines may be subjected to various electrical and (or) mechanical faults [1]. These faults cause decadence or disablement of the motor [2]. In LIMs, this problem is more special, because the secondary is paved without any preservative from external factors. In other words, all parts of the rotary machine is limited and protected with its frame, while the secondary of LIMs has no option for the mentioned aim in the most cases. In addition, the electrical failures could occur in LIMs like as source and coils short circuits, breaking the secondary plate, unbalanced power supply, etc. [1]. The mechanical failures in LIMs consist contact between primary and secondary, eccentricity of motor, etc. Based on the reference researches [1]–[4], the most common faults in a Rotary Induction Motor (RIM) are related to the bearing (∼ 70 %), stator windings (∼ 20 %), and rotor bars (5–10 %). In other hand, there is no bearing in LIM that increases its advantage and interest in more applications. Therefore, we could classify the LIM faults into primary (stator) windings and secondary conductor sheet. In this work, the fault detection of LIMs is contributed for the first time and the results are analyzed for future designs.

B. LITERATURE REVIEW

There are various recent studies have proposed novel detection methods for different faults. In [3], the authors

The associate editor coordinating the review of this manuscript and approving it for publication was R. K. Saket.

prepared a novel fault detection method based on Hilbert Transform (HT) for multi–broken rotor bars in a three-phase Rotary Induction Motor (RIM). A novel method based on extraction of acoustic signals from a single-phase RIM is developed in [4], which tested in various faults. The motor current signature is used in [5] for bearing fault detection that noises are eliminated with Wiener filter and the spectral analysis is done with Direct Wavelet Transform (DWT). In other work [6], infrared thermography technique–color based is used for inter turn faults diagnosis. The variable speed RIM is considered in [7] for broken bar fault detection using DWT and energy eigen values. In [8], deep network-based features of thermograms base on thermal images is used for fault detection of a real three-phase RIM. Authors of [9] have used the Kalman Filter (KF) based algorithm, which extract the current and voltage signatures, for diagnosis of stator inter turn faults of RIMs.

With considering the literature of fault diagnosis methods, they could classified in three important parts as signal processing, machine learning, and artificial intelligent algorithms, which the first method is widely used in the fault detection of electrical machines. The recent signal processing methods such as acoustic signals analysis [4], [10], [11], the vector space decomposition approach [12], KF based approaches [9], [13], various Fourier Transforms (FTs) [14]–[16], the HT [3], [17], the Hilbert–Huang Transform (HHT) [18]–[21], space pattern recognition [22], various Wavelet Transforms (WT) [5], [7], [23] or combined methods [24]–[26], etc., the machine learning based approaches such as Random Forest (RF) algorithm [27], fuzzy-Bayesian [28], Support Vector Machine (SVM) [29], etc., and artificial intelligent algorithms such as Artificial Neural Network (ANN) methods [30], [31] have been proposed and used in the RIM fault detection problems.

The above researches are based on the methods that needs several tests and to verify the results, even though the method is robust. The Finite Element Method (FEM) is a powerful solution to verify these results. This method has been utilized for design and analysis of electrical machines in plenty of applications. However, it recently is also applied in the various fault detection problems. Liang *et al.* in [32] have reviewed studies that have used FEM in the fault detection of RIMs. Corresponding to this reference, the all proposed techniques could be classified into three main categories as only FEM, FEM and signal processing methods, and FEM and machine learning algorithms. The various failures could be detected using the assessment and justifying of machine parameters [33]. In [34], the authors use the FEM for inter–turn short circuit of stator winding of RIM by extracting the harmonic of the flux leakage. The bearing fault of a RIM by using the investigation of a relation between the vibration and current is studied in [35] that FEM is the solution method. The thermal effects of broken bars in RIM is studied in [36] using FEM, which it could estimate the number of broken bars with assessment of the stator current. In [37], a method based on FEM and modified winding function is used for fault detection with considering the magnetic saturation of RIM. The online fault diagnosis using FEM has been proposed in [38], which prepare the current density of bars as a function of their position. The second method, FEM with signal processing, is more common and widely is used in the literature. Fault detection of the broken bars [39]–[42], bearing failures [43]–[45], and the short circuit of stator windings [46]–[49] are the most problems that studied with researchers. Finally, the FEM with machine learning and other techniques has been in few references, such as broken bars with FFT, Yule Walker Estimate by Auto Regression (YUL-AR), and Matching Pursuit (MP) [50], bearing problems with SVM [51], and rotor asymmetry and inter-turn stator winding short circuits by sparse subspace learning (SSL) [52].

As confirmed in the mentioned papers, the fault diagnosis problem will be more accurate with using of FEM and signal process algorithms. In addition, the HHT and WT are better and faster than other method [19], [23].

C. PAPER CONTRIBUTIONS

In this paper, an HTS–SLIM is considered to investigate the sufferable and sustainability of them under faults by electrical and mechanical analysis. In addition, a method based on 3D FEM and HHT is employed for fault detection problem. In essence, the main contributions of this paper are listed as below:

- Dynamic analysis of HTS–SLIM under different electrical and mechanical faults to assess its performance, which has not been done before;
- Employment of fault detection solution on HTS–SLIM and proposed the modeling formulation for this aim, which no research has been found in this case;
- The 3D FEM and HHT make a new combined method that is applied for the fault diagnosis problem, which could proposed a novel strategy for other applications;
- The results show that the HTS–SLIM could suffer the short circuit, due to the high capacity of current density in HTS tapes.

II. MODELING OF FAULTY HTS-SLIM

A. RESISTANCE CALCULATION OF SECONDARY SHEET

In the flat solid aluminum, its active resistance (R_{solid}) under normal condition is calculated as follow:

$$R_{solid} = \frac{\rho.L}{d.w} \ (\Omega) \tag{1}$$

where, ρ is the is the aluminum resistivity, which is equal to 2.82e–8 [Ω.m], L is the motor length, d and w is the thickness and width of sheet, respectively. The value of resistance is highly depended to ρ, which means that if sheet is broken in active part, the value of resistance will be changed. The 3D model of flat solid sheet under a broken fault is presented in Fig. 1.

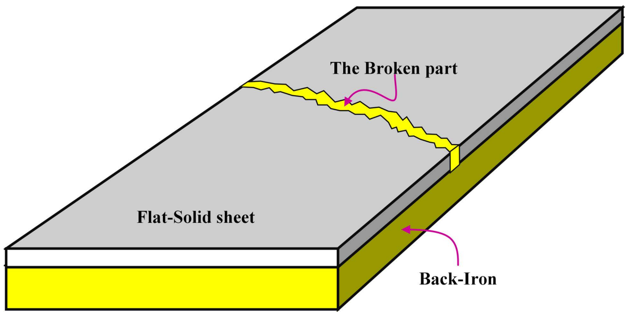

FIGURE 1. The broken sheet fault in the flat solid secondary of HTS- SLIM.

B. PRIMARY WINDINGS UNDER SHORT CIRCUIT FAULTS

1) DYNAMIC MODELING OF SLIM IN HEALTHY CONDITION

The equivalent circuit of a SLIM is shown in Fig. 2. In order to model the SLIM with considering the end effects, the obtained model will be different from RIMs. The relation of linear and angular speeds is as follows:

$$V_r = \frac{\tau}{\pi}\omega_r \tag{2}$$

where, τ is the pole pitch, ω_r is the angular speed [rad.s^{-1}], and V_r is the linear speed [m.s^{-1}].

Due to linear motion of SLIM as well as creation and abolition of magnetic field in the ends of motor, the eddy currents are appeared in the secondary sheets. Based on Fig. 2, a new series resistance (R_m), which indicates the eddy current loss, is connected to magnetizing inductance. The 3-phase relations of voltage–current for both primary and secondary under non–faulted condition are defined by (3). In this matrix, the hypothetical windings are considered for the secondary conductor.

$$\begin{bmatrix} v_{a1} \\ v_{b1} \\ v_{c1} \\ v'_{a2} \\ v'_{b2} \\ v'_{c2} \end{bmatrix} = \begin{bmatrix} R_{t1} & 0 & 0 & R_m & 0 & 0 \\ 0 & R_{t1} & 0 & 0 & R_m & 0 \\ 0 & 0 & R_{t1} & 0 & 0 & R_m \\ R_m & 0 & 0 & R_{t2} & 0 & 0 \\ 0 & R_m & 0 & 0 & R_{t2} & 0 \\ 0 & 0 & R_m & 0 & 0 & R_{t2} \end{bmatrix} \begin{bmatrix} i_{a1} \\ i_{b1} \\ i_{c1} \\ i'_{a2} \\ i'_{b2} \\ i'_{c2} \end{bmatrix} + \frac{d}{dt}\begin{bmatrix} \lambda_{a1} \\ \lambda_{b1} \\ \lambda_{c1} \\ \lambda'_{a2} \\ \lambda'_{b2} \\ \lambda'_{c2} \end{bmatrix} \tag{3}$$

where, $R_{t1} = R_1 + R_m$, $R_{t2} = R'_2 + R_m$, v_{i1} and v'_{i2} are the primary voltage and secondary voltage transferred to primary, respectively, i_{i1} and i'_{i2} are the primary current and secondary current transferred to primary, respectively, and λ_{i1} and λ'_{i2} are the primary flux and secondary flux transferred to primary, respectively, which $i = \{a, b, c\}$ indicates the phase index. The primary and secondary fluxes could be rewritten in terms of inductances and currents as follows:

$$\begin{bmatrix} \boldsymbol{\lambda}_1^{abc} \\ \boldsymbol{\lambda}'_2abc \end{bmatrix} = \begin{bmatrix} \mathbf{L}_{11}^{abc} + \mathbf{L}_{11}^{abc} & \mathbf{L}_{12}^{abc} \\ \mathbf{L}_{21}^{abc} & \mathbf{L}_{l2}^{\prime abc} + \mathbf{L}_{22}^{\prime abc} \end{bmatrix} \begin{bmatrix} \mathbf{i}_1^{abc} \\ \mathbf{i}_2^{\prime abc} \end{bmatrix} \tag{4}$$

where:

$$\lambda_1^{abc} = [\lambda_{a1}, \lambda_{b1}, \lambda_{c1}]^T \tag{5}$$

$$\boldsymbol{\lambda}'^{abc}_2 = \left[\lambda'_{a2}, \lambda'_{b2}, \lambda'_{c2}\right]^T \tag{6}$$

$$\mathbf{i}_1^{abc} = [i_{a1}, i_{b1}, i_{c1}]^T \tag{7}$$

$$\mathbf{i}'^{abc}_2 = \left[i'_{a2}, i'_{b2}, i'_{c2}\right]^T \tag{8}$$

$$\mathbf{L}_{l1}^{abc} = \begin{bmatrix} L_{l1} & 0 & 0 \\ 0 & L_{l1} & 0 \\ 0 & 0 & L_{l1} \end{bmatrix} \tag{9}$$

$$\mathbf{L}'^{abc}_{l2} = \begin{bmatrix} L'_{l2} & 0 & 0 \\ 0 & L'_{l2} & 0 \\ 0 & 0 & L'_{l2} \end{bmatrix} \tag{10}$$

$$\mathbf{L}_{11}^{abc} = f(Q)\begin{bmatrix} L_{11} & L_{1m} & L_{1m} \\ L_{1m} & L_{11} & L_{1m} \\ L_{1m} & L_{1m} & L_{11} \end{bmatrix} \tag{11}$$

$$\mathbf{L}'^{abc}_{22} = f(Q)\begin{bmatrix} L'_{22} & L'_{2m} & L'_{2m} \\ L'_{2m} & L'_{22} & L'_{2m} \\ L'_{2m} & L'_{2m} & L'_{22} \end{bmatrix} \tag{12}$$

$$\begin{aligned} \mathbf{L}_{12}^{abc} &= [\mathbf{L}_{21}^{abc}]^T = L_{12} f(Q) \\ &\times \begin{bmatrix} \cos\theta_r & \cos\left(\theta_r + \frac{2\pi}{3}\right) & \cos\left(\theta_r - \frac{2\pi}{3}\right) \\ \cos\left(\theta_r - \frac{2\pi}{3}\right) & \cos\theta_r & \cos\left(\theta_r + \frac{2\pi}{3}\right) \\ \cos\left(\theta_r + \frac{2\pi}{3}\right) & \cos\left(\theta_r - \frac{2\pi}{3}\right) & \cos\theta_r \end{bmatrix} \end{aligned} \tag{13}$$

In (4)–(13), L_{l1} and L'_{l2} are the leakage inductance of primary and secondary transferred to primary, L_{11} and L'_{22} are the magnetizing inductance of primary and secondary transferred to primary, L_{1m} and L'_{2m} are the mutual inductance of primary windings and secondary windings transferred to primary, and L_{12} is the maximum mutual inductance between the primary and secondary windings. Also, the relation between all inductances is assumed as $L_{11} = L'_{22} = -2L_{1m} = -2L'_{2m}$ in healthy condition. In (13), θ_r is the difference angle of phase "a" between the primary and secondary, which could find as follows:

$$\theta_r = \int \omega_r dt + \theta_r(0) \tag{14}$$

The function $f(Q)$ in (11)–(13) is related to inductance matrices (also shown in Fig. 2), and is defined as follows:

$$f(Q) = 1 - \frac{1 - e^{-Q}}{Q} \tag{15}$$

where, Q is the normalized length of motor. Let's reform the above relations in "dq0" reference. The matrix of (3) could be rewritten as follow:

$$\begin{cases} \mathbf{v}_1^{abc} = p\boldsymbol{\lambda}_1^{abc} + \left(\mathbf{R}_1^{abc} + \mathbf{R}_m^{abc}\right)\mathbf{i}_1^{abc} + \mathbf{R}_m^{abc}\mathbf{i}_2^{\prime abc} \\ \mathbf{v}_2^{\prime abc} = p\boldsymbol{\lambda}_2^{\prime abc} + \left(\mathbf{R}_2^{\prime abc} + \mathbf{R}_m^{abc}\right)\mathbf{i}_2^{\prime abc} + \mathbf{R}_m^{abc}\mathbf{i}_1^{abc} \end{cases} \tag{16}$$

where, p denotes the derivative operator, and $\mathbf{R}_m^{abc} = R_m\mathbf{I}_3$, which $\mathbf{I}_3$ is the identity matrix with rank of 3. With applying the Park transform in (16), the final relation could be obtained as written in (17), as shown at the bottom of the next page. Besides, with doing similar calculation on (4), the transformed fluxes to "dq0" reference are obtained as follows:

$$\begin{cases} \lambda_1^{qd0} = \begin{bmatrix} L_{t1} & 0 & 0 \\ 0 & L_{t1} & 0 \\ 0 & 0 & L_{l1} \end{bmatrix} \mathbf{i}_1^{qd0} + \begin{bmatrix} L_z & 0 & 0 \\ 0 & L_z & 0 \\ 0 & 0 & 0 \end{bmatrix} \mathbf{i}_2^{\prime} qd0 \\ \lambda_2^{\prime qd0} = \begin{bmatrix} L'_{t2} & 0 & 0 \\ 0 & L'_{t2} & 0 \\ 0 & 0 & L'_{l2} \end{bmatrix} \mathbf{i}_2^{\prime\prime d0} + \begin{bmatrix} L_z & 0 & 0 \\ 0 & L_z & 0 \\ 0 & 0 & 0 \end{bmatrix} \mathbf{i}_1^{qd0} \end{cases} \tag{18}$$

where:

$$\begin{cases} L_{t1} = L_{l1} + L_m f(Q) \\ L'_{t2} = L'_{l2} + L_m f(Q) \\ L_z = L_m f(Q) \end{cases} \tag{19}$$

The equivalent circuit of the dynamic model for SLIM in heathy mode is presented in Fig. 3. Finally, the output thrust could be calculated as follows:

$$\begin{aligned} F_e &= \frac{3\pi}{2\tau}\left(\lambda_{d1}i_{q1} - \lambda_{q1}i_{d1}\right) = \frac{3\pi}{2\tau}\left(\lambda'_{q2}i'_{d2} - \lambda'_{d2}i'_{q2}\right) \\ &= \frac{3\pi}{2\tau}L_m f(Q)\left(i'_{d2}i_{q1} - i'_{q2}i_{d1}\right) \end{aligned} \tag{20}$$

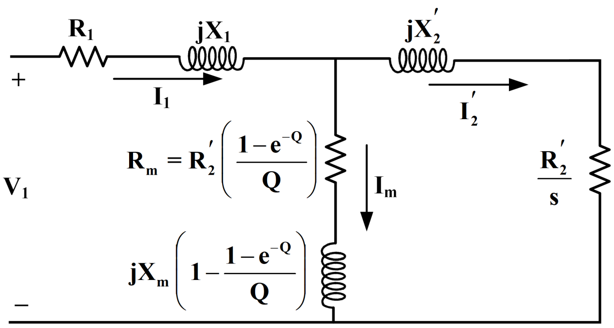

FIGURE 2. The equivalent circuit of a SLIM in non-faulty operation.

2) SLIM MODELING UNDER WINDING FAULTS

The schematic of 3-phase physical windings under inter-turn short circuit is presented in Fig. 4. The turn number of short circuit and safe coils in phase "b" is considered as N_{b2} and N_{b1}, respectively, which $N_b = N_{b1} + N_{b2}$ is the total turn number of winding of phase "b". Also, in other two phases, the similar relation is confirmed: $N_a = N_{a1} + N_{a2}$,

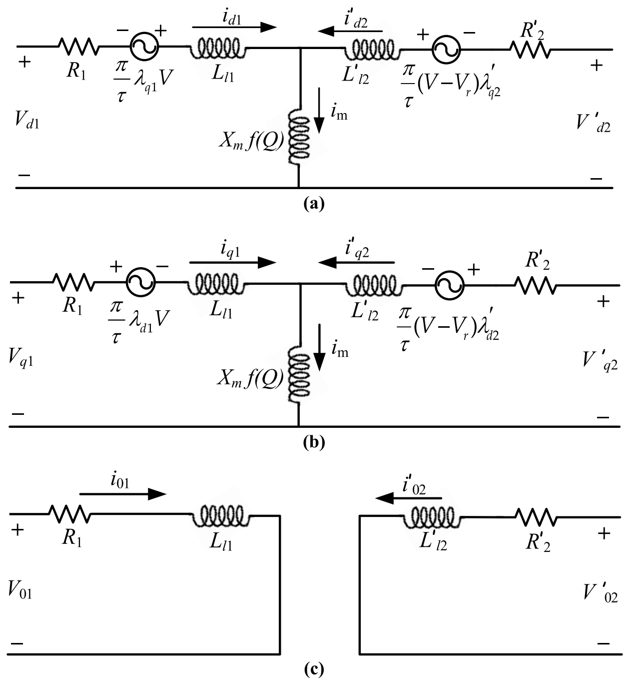

FIGURE 3. The equivalent circuit of a SLIM in non-faulty operation considering the end-effects: (a) For "d" axis, (b) For "q" axis, and (c) For "0" axis.

$N_c = N_{c1} + N_{c2}$. The severity factor of fault could be defined as $\chi = N_{b2}/N_b$.

From the basic of electrical machines, the leakage and magnetizing inductances are obtained as follows [53]:

$$L_{l1} = \frac{N_b^2}{\Re_{l1}} \tag{21}$$

$$L_{1m} = \frac{N_b^2}{\Re_{1m}} \tag{22}$$

where, $\Re_{1m}$ and $\Re_{l1}$ are the magnetizing and leakage reluctance paths of inductances L_{1m} and L_{l1}, respectively. Moreover, the self–inductance of each coil of phase "b" in Fig. 4 (b) is defined as follows:

$$\begin{cases} L_{b1} = L_{lb1} + L_{mb1} = \dfrac{N_{b1}^2}{\Re_{b1}} + \dfrac{N_{b1}^2}{\Re_{mb1}} \\ L_{b2} = L_{lb2} + L_{mb2} = \dfrac{N_{b2}^2}{\Re_{lb2}} + \dfrac{N_{b2}^2}{\Re_{mb2}} \end{cases} \tag{23}$$

With assumed the equal magnetizing reluctances for both coils ($\Re_{mb1} = \Re_{mb2} = \Re_{1m}$) [54]. The final relation of inductances are rendered in (24). In addition, the mutual inductance (M) of coils "b1" and "b2" is calculated by (25).

$$\begin{cases} L_{b1} = \dfrac{(1-\chi)^2 N_b^2}{\Re_{lb1}} + \dfrac{(1-\chi)^2 N_b^2}{\Re_{1m}} \\ = \dfrac{(1-\chi)^2 N_b^2}{\Re_{lb1}} + (1-\chi)^2 L_{1m} \\ L_{b2} = \dfrac{\chi^2 N_b^2}{\Re_{lb2}} + \dfrac{\chi^2 N_b^2}{\Re_{1m}} = \dfrac{\chi^2 N_b^2}{\Re_{lb2}} + \chi^2 L_{1m} \end{cases} \tag{24}$$

$$\begin{cases} L_b = L_{l1} + L_{1m} = L_{b1} + L_{b2} + 2M \\ M = \dfrac{N_{b1}N_{b2}}{\Re_{1m}} = \chi(1-\chi)L_{1m} \end{cases} \tag{25}$$

With simplification of (25), with replacing (23) and (24), the following relation is obtained:

$$L_{l1} = L_{lb1} + L_{lb2} \tag{26}$$

The following proportionality rule is also established:

$$\chi^2 L_{b1} = (1-\chi)^2 L_{b2} \tag{27}$$

Therefore, with considering the (26) and (27), the following relation between leakage inductance is obtained [54], [55]:

$$\begin{cases} L_{lb1} = \dfrac{(1-\chi)^2}{1-2\chi+2\chi^2} L_{l1} = k_{lb1} L_{l1} \\ L_{lb1} = \dfrac{\chi^2}{1-2\chi+2\chi^2} L_{l1} = k_{lb2} L_{l1} \end{cases} \tag{28}$$

The flux matrix in the faulty motor, with considering an coil short circuit fault in the primary winding of phase "b" will be changed as follow:

$$\begin{bmatrix} \boldsymbol{\lambda}_1^{f-abc} \\ \lambda_2^{\prime f-abc} \end{bmatrix} = \begin{bmatrix} \mathbf{L}_{l1}^{f-abc} + \mathbf{L}_{11}^{f-abc} & \mathbf{L}_{12}^{f-abc} \\ \mathbf{L}_{21}^{f-abc} & \mathbf{L}_{l2}^{\prime abc} + \mathbf{L}_{22}^{\prime abc} \end{bmatrix} \begin{bmatrix} \mathbf{i}_1^{f-abc} \\ \mathbf{i}_2^{\prime} abc \end{bmatrix} \tag{29}$$

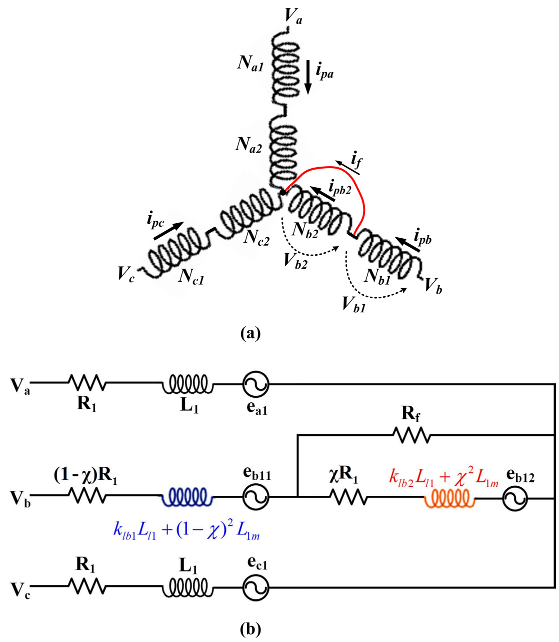

FIGURE 4. The equivalent circuit of a SLIM in non–faulty operation (a) The main reference (3-phase); (b) In the "dq0" reference.

where (30)–(34), as shown at the bottom of the page. (35), as shown at the bottom of page 7.

$$\begin{cases} \mathbf{v}_1^{qd0} = p\lambda_1^{qd0} + \left(\dfrac{\pi V}{\tau}\right) \begin{bmatrix} 0 & 1 & 0 \\ -1 & 0 & 0 \\ 0 & 0 & 0 \end{bmatrix} \lambda_1^{qd0} + \left(\mathbf{R}_1^{qd0} + \mathbf{R}_m^{qd0}\right) \mathbf{i}_1^{qd0} + \mathbf{R}_m^{qd0} \begin{bmatrix} \cos\theta_r & -\sin\theta_r & 0 \\ -\sin\theta_r & \cos\theta_r & 0 \\ 0 & 0 & 1 \end{bmatrix} \mathbf{i}_2^{\prime qd0} \\ \mathbf{v}_2^{\prime qd0} = p\boldsymbol{\lambda}_2^{\prime qd0} + \left(\dfrac{\pi (V - V_r)}{\tau}\right) \begin{bmatrix} 0 & 1 & 0 \\ -1 & 0 & 0 \\ 0 & 0 & 0 \end{bmatrix} \lambda_1^{qd0} + \left(\mathbf{R}_2^{\prime qd0} + \mathbf{R}_m^{qd0}\right) \mathbf{i}_2^{\prime qd0} + \mathbf{R}_m^{qd0} \begin{bmatrix} \cos\theta_r & -\sin\theta_r & 0 \\ -\sin\theta_r & \cos\theta_r & 0 \\ 0 & 0 & 1 \end{bmatrix} \mathbf{i}_1^{qd0} \end{cases} \tag{17}$$

$$\lambda_1^{f-abc} = \left[\lambda_{a1}^f, \lambda_{b11}^f, \lambda_{b12}^f, \lambda_{c1}^f\right]^T \tag{30}$$

$$\boldsymbol{\lambda}_2^{\prime f-abc} = \left[\lambda_{a2}^{\prime f}, \lambda_{b2}^{\prime f}, \lambda_{c2}^{\prime f}\right]^T \tag{31}$$

$$\mathbf{i}_1^{f-abc} = [i_{a1}, i_{b11}, i_{b12}, i_{c1}]^T \tag{32}$$

$$\mathbf{L}_{l1}^{f-abc} = L_{l1} \begin{bmatrix} 1 & 0 & 0 & 0 \\ 0 & k_{lb1} & 0 & 0 \\ 0 & 0 & k_{lb2} & 0 \\ 0 & 0 & 0 & 1 \end{bmatrix} \tag{33}$$

$$\mathbf{L}_{11}^{f-abc} = L_{11} f(Q) \begin{bmatrix} 1 & -\dfrac{1-\chi}{2} & -\dfrac{\chi}{2} & -\dfrac{1}{2} \\ -\dfrac{1-\chi}{2} & (1-\chi)^2 & \chi(1-\chi) & -\dfrac{1-\chi}{2} \\ -\dfrac{\chi}{2} & \chi(1-\chi) & \chi^2 & -\dfrac{\chi}{2} \\ -\dfrac{1}{2} & -\dfrac{1-\chi}{2} & -\dfrac{\chi}{2} & 1 \end{bmatrix} \tag{34}$$

In addition, the relation of voltages in faulty mode for SLIM based on (16) is calculated with follows (36), as shown at the bottom of the next page, where:

$$\mathbf{R}_1^{f-abc} = R_1 \begin{bmatrix} 1 & 0 & 0 & 0 \\ 0 & 1-\chi & 0 & 0 \\ 0 & 0 & \chi & 0 \\ 0 & 0 & 0 & 1 \end{bmatrix} \tag{37}$$

$$\mathbf{R}_{m1}^{f-abc} = R_m \begin{bmatrix} 1 & 0 & 0 & 0 \\ 0 & 1-\chi & 0 & 0 \\ 0 & 0 & \chi & 0 \\ 0 & 0 & 0 & 1 \end{bmatrix} \tag{38}$$

$$\mathbf{R}_{m2}^{f-abc} = R_m \begin{bmatrix} 1 & 0 & 0 \\ 0 & 1-\chi & 0 \\ 0 & \chi & 0 \\ 0 & 0 & 1 \end{bmatrix} \tag{39}$$

The relations of voltages and fluxes in "dq0" reference will be reformed as (40), as shown at the bottom of the next page. In (40), $\mathbf{R}_x^{dq} = R_x$ diag[1 1], and $x = \{1, m\}$. Also, $\mathbf{v}_1^{f-dq} = [v_q v_d]^{\mathrm{T}}$, and $\mathbf{i}_1^{dq} = [i_q i_d]^{\mathrm{T}}$. The flux matrix of primary and secondary also modified as written in (41), as shown at the bottom of the next page.

Finally, the output thrust in faulty mode of SLIM could be calculated as follows:

$$F_e = \frac{3\pi}{2\tau} L_m f(Q) \left(i'_{d2} i_{q1} - i'_{q2} i_{d1} \right) - \frac{\pi}{\tau} \chi L_m f(Q) \left(i'_{q2} i_f \right) \tag{42}$$

III. THE HILBERT–HUANG TRANSFORM

The HHT, first, is introduced by Huang and Shen [56], which is applied for multi–component signals. This signal processing technique is based on the signal disintegration within two forms as empirical modes with their representation into a set of complex detection manner [21]. First, we supposed a time–based signal as $X(t)$, which is the real part of a complex analytic signal $Z(t) = X(t) + jY(t)$, which $Y(t)$ is the HT of $X(t)$, and is defined as:

$$\mathcal{H}(X(t)) = Y(t) = \frac{1}{\pi} PV \int_{-\infty}^{+\infty} \frac{X(\tau)}{t-\tau} d\tau \tag{43}$$

In (43), PV is the principal value of the singular integral [56]. Therefore, the analytic signal, $Z(t)$, could be reformed as follows:

$$\begin{cases} Z(t) = X(t) + jY(t) = A(t) \times \exp(j\varphi(t)) \\ A(t) = \sqrt{X^2(t) + Y^2(t)} \\ \varphi(t) = \arctan\left(Y(t)X^{-1}(t)\right) \end{cases} \tag{44}$$

where, $A(t)$ and $\varphi(t)$ are the instantaneous amplitude and phasor function, respectively. Therefore, the frequency could be obtained with derivation of phasor function, as follow:

$$\omega(t) = \frac{d}{dt}\varphi(t) \tag{45}$$

A. INTRINSIC MODE FUNCTION COMPONENTS

By employing the local limitation condition, in order to substitute the global limitations, a new instantaneous frequency is prepared with HT. Therefore, an Intrinsic Mode Function (IMF) could be introduced with the follow conditions [20]:

1) The number of extrema and zero-crossing points should be equal, or differ by one at most;
2) For all points, mean value of envelope calculated with local minimum as well as local maximum should be zero.

With considering the IMF, the relation defined in (45) could obtain the best frequency. An IMF in following the HT could be shown with (44). With applying the FT on $Z(t)$, the results will be as follows:

$$\mathcal{F}(Z(t)) = \int_{-\infty}^{+\infty} A(t) \times \exp(j(\varphi(t) - \omega t))dt \tag{46}$$

Then, the maximum contribution of $W(\omega)$ will be obtained using the frequency assuring the follow condition:

$$\frac{d}{dt}(\varphi(t) - \omega t) = 0 \tag{47}$$

This manner is better defining than zero-crossing for instantaneous frequency. An IMF shows an easy swing mode as a peer to the simple harmonic function, but it is works more general. In order to replacing the constant components of signals, the IMF could render a time-based variable frequency and amplitude.

B. THE EMPIRICAL MODE DECOMPOSITION

For decomposing a complicated time-variable signal to IMF components, Huang *et al.* [56] have prepared the Empirical Mode Decomposition (EMD) method, which is based on local feature of the signal. The main contribution of this method is that the lower and upper bands (envelopes) of each signal $X(t)$ should be defined with cubic spline line to cover all data. Then, the mean of these envelopes is considered as $M_1(t)$. The ideal first component of IMF could be defined as $h_1(t) =$ X(t) – $M_1(t)$. However, in order to reach the final value of the IMF component, this processes should repeat until to eliminate the error signals as follows:

$$\sum_t \frac{(h_k(t) - h_{k-1}(t))^2}{(h_{k-1}(t))^2} < [0.2 \sim 0.3] \tag{48}$$

The EMD find the next IMF component using the above process. If $c_1(t)$ is considered as the first IMF, the rest of data will be calculated as $r_1(t) = X(t)–c_1(t)$. This technique should be continued till the last rest data ($r_n(t)$) consists at most one local extrema:

$$\begin{cases} r_1(t) = X(t) - c_1(t); \\ r_2(t) = r_1(t) - c_2(t); \\ \vdots \\ r_n(t) = r_{n-1}(t) - c_n(t); \end{cases} \Rightarrow X(t) = r_n(t) + \sum_{i=1}^{n} c_i(t) \tag{49}$$

In (49), there are n components of the IMF, i.e. $c_1(t)$, $c_2(t), \ldots, c_n(t)$, that the first IMF ($c_1(t)$) contains the largest frequencies in the main signal $X(t)$.

C. THE HILBERT SPECTRUM

The HT described the IMF components in (49). Then, the main signal could be express as follows by using (44) and (45):

$$\begin{aligned} X(t) &= \mathrm{Re}\,[Z(t)] = \mathrm{Re}\left[\sum_{i=1}^{n}[A_i(t) \times \exp(j\varphi_i(t))]\right] \\ &= \mathrm{Re}\left[\sum_{i=1}^{n}\left[A_i(t) \times \exp\left(j \int_{-\infty}^{t} \omega_i(t)dt\right)\right]\right] \end{aligned} \tag{50}$$

The relation defined in (50) consists of both amplitude and instantaneous frequency that could be represented in

$$\mathbf{L}_{12}^{f-abc} = [\mathbf{L}_{21}^{f-abc}]^T = L_{12}f(Q)\begin{bmatrix} \cos\theta_r & \cos\left(\theta_r + \frac{2\pi}{3}\right) & \cos\left(\theta_r - \frac{2\pi}{3}\right) \\ (1-\chi)\cos\left(\theta_r - \frac{2\pi}{3}\right) & (1-\chi)\cos\theta_r & (1-\chi)\cos\left(\theta_r + \frac{2\pi}{3}\right) \\ \chi\cos\left(\theta_r - \frac{2\pi}{3}\right) & \chi\cos\theta_r & \chi\cos\left(\theta_r + \frac{2\pi}{3}\right) \\ \cos\left(\theta_r + \frac{2\pi}{3}\right) & \cos\left(\theta_r - \frac{2\pi}{3}\right) & \cos\theta_r \end{bmatrix} \tag{35}$$

$$\begin{bmatrix} \mathbf{v}_1^{f-abc} \\ \mathbf{v}_2'^{abc} \end{bmatrix} = p\begin{bmatrix} \lambda_1^{f-abc} \\ \boldsymbol{\lambda}_2'^{f-abc} \end{bmatrix} + \begin{bmatrix} \mathbf{R}_1^{f-abc} + \mathbf{R}_{m1}^{f-abc} & \mathbf{R}_{m2}^{f-abc} \\ \left[\mathbf{R}_{m2}^{f-abc}\right]^{\mathrm{T}} & \mathbf{R}_2'^{abc} + \mathbf{R}_m^{abc} \end{bmatrix}\begin{bmatrix} \mathbf{i}_1^{f-abc} \\ \mathbf{i}_2'^{abc} \end{bmatrix} \tag{36}$$

$$\begin{cases} \mathbf{v}_1^{f-qd} = p\boldsymbol{\lambda}_1^{dq} + \left(\frac{\pi V}{\tau}\right)\begin{bmatrix} 0 & 1 \\ -1 & 0 \end{bmatrix}\boldsymbol{\lambda}_1^{dq} + \left(\mathbf{R}_1^{dq} + \mathbf{R}_m^{qd}\right)\mathbf{i}_1^{qd} + \mathbf{R}_m^{qd}\begin{bmatrix} \cos\theta_r & -\sin\theta_r \\ -\sin\theta_r & \cos\theta_r \end{bmatrix}\mathbf{i}_2'^{d} - \frac{2}{3}\chi\begin{bmatrix} R_1 \\ R_1 \end{bmatrix} i_f \\ \mathbf{v}_1^{f-0} = p\lambda_1^0 + (R_1 + R_m)\, i_1^0 + R_m i_2' 0 - \frac{1}{3}\chi R_1 i_f \\ \mathbf{v}_2'^{f-qd0} = p\boldsymbol{\lambda}_2'^{f-qd0} + \left(\frac{\pi\,(V - V_r)}{\tau}\right)\begin{bmatrix} 0 & 1 & 0 \\ -1 & 0 & 0 \\ 0 & 0 & 0 \end{bmatrix}\boldsymbol{\lambda}_1^{f-qd0} + \left(\mathbf{R}_2'^{qd0} + \mathbf{R}_m^{qd0}\right)\mathbf{i}_2'^{qd0} \\ + \mathbf{R}_m^{qd0}\begin{bmatrix} \cos\theta_r & -\sin\theta_r & 0 \\ -\sin\theta_r & \cos\theta_r & 0 \\ 0 & 0 & 1 \end{bmatrix}\mathbf{i}_1^{f-qd0} \end{cases} \tag{40}$$

$$\begin{cases} \lambda_1^{f-qd0} = \begin{bmatrix} L_{t1} & 0 & 0 \\ 0 & L_{t1} & 0 \\ 0 & 0 & L_{l1} \end{bmatrix}\mathbf{i}_1^{qd0} + \begin{bmatrix} L_z & 0 & 0 \\ 0 & L_z & 0 \\ 0 & 0 & 0 \end{bmatrix}\mathbf{i}_2'^{qd0} + \chi\begin{bmatrix} \frac{L_{11}}{2} \\ \frac{-\chi L_{l1}}{1 - 2\chi + \chi^2} - L_{11} \\ \frac{L_{11}}{2} \end{bmatrix} i_f \\ \boldsymbol{\lambda}_2'^{f-qd0} = \begin{bmatrix} L_{t2}' & 0 & 0 \\ 0 & L_{t2}' & 0 \\ 0 & 0 & L_{l2}' \end{bmatrix}\mathbf{i}_2'^{qd0} + \begin{bmatrix} L_z & 0 & 0 \\ 0 & L_z & 0 \\ 0 & 0 & 0 \end{bmatrix}\mathbf{i}_1^{qd0} - L_{11}\begin{bmatrix} \cos(\theta_r) \\ \cos(\theta_r + \frac{2\pi}{3}) \\ \cos(\theta_r - \frac{2\pi}{3}) \end{bmatrix} i_f \end{cases} \tag{41}$$

time- frequency plane [18]. This distribution is introduced as the Hilbert–Huang Spectrum (HHS), $\mathcal{H}(\omega, t)$, as follow:

$$\mathcal{H}(\omega, t) = \mathrm{Re}\left[\sum_{i=1}^{n}\left[A_i(t) \times \exp\left(j\int_{-\infty}^{t}\omega_i(t)dt\right)\right]\right] \quad (51)$$

The marginal spectrum is also defined as follow:

$$h(\omega) = \int_{0}^{T}\mathcal{H}(\omega, t)dt \quad (52)$$

The reviewed EMD method with the HHS analysis are called HHT. The first method extracts the IMF components and the second technique finds the instantaneous frequency of the extracted IMF component using the HT.

IV. THE SIMULATION RESULTS

A. THE PROPERTIES OF THE STUDIED HTS–SLIM

In this paper, an HTS–SLIM is considered to compare its behavior and sustainability under two faults (broken secondary and inter-turn short circuit). The 3D model of this motor is shown in Fig. 5. In addition, the main features of this motor are listed in Table 1 [57]. The considered tapes for windings are type II superconductors with material of Bi–2223.

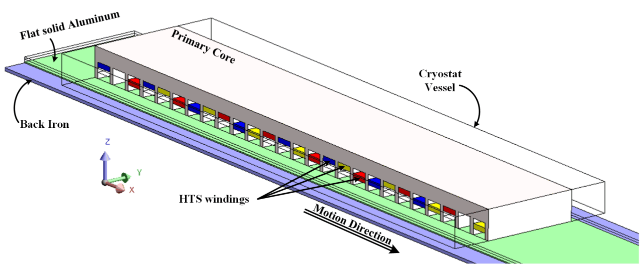

FIGURE 5. The 3D FEM model of studied structure of HTS–SLIM.

B. THE FAULT DETECTION RESULTS

1) THE BROKEN SECONDARY

The first analysis of the broken secondary sheet is related to its current density and flux density, which are shown in Fig. 6. In Fig. 6 (a), the distribution of current density before fault is shown that maximum value is reached 16 MA.m^{-2}. However, when the primary is enter into broken sheet, the maximum current density is increased to 103 MA.m^{-2} as shown in Fig. 6 (b).

In addition, this value is related to the boundary of broken region. Worse still, the loss power will be increased and therefore, the energy of machine increase until cross over this region. The distributions of flux density in secondary sheet for before and on the broken part are also shown in Fig. 6 (c) and Fig. 6 (d), respectively. It is cleared that the maximum flux density is increased from 0.5 T to 1.9 T, which show about 4 times increment.

The variation of speed and thrust of motor is rendered in Fig. 7. As shown in this figure, the first level of thresholds

TABLE 1. The main features of the studied HTS–SLIM.

Parameter	Symbol	unit	Value
Input frequency	f	Hz	10
RMS of 3∅ current sources	I_P	A	25
Turns number of each coil	N	-	240
Windings connection model	-	-	Y
Number of poles	p	-	8
Pole pitch	τ	mm	177.6
Air gap	g	mm	12
Synchronous speed	V_s	m.s^{-1}	3.5
Length of the primary core	W_p	mm	1551
Height of the primary core	H_p	mm	80
Width of the primary core	b_p	mm	250
Slot width	b_s	mm	47.2
Slot depth	h_s	mm	42
Tooth width	w_t	mm	12
Conducting plate width	W_c	mm	330
Conducting plate thickness	d	mm	3
Back-iron width	W_b	mm	450
Back-iron thickness	h_b	mm	8

of thrust is defined between 0 to 3 kN. Moreover, the first level of threshold for speed is defined as 0 to 3.8 m.s^{-1}. Due to higher current density in broken region, the thrust also should be increased. In addition the speed of the motor is also increased in this region. Thrust is varied between –2 kN and +6 kN in broken sheet region and speed increased to 5 m.s^{-1}. The both of speed and thrust have infringed the upper threshold levels. In addition, thrust have negative values in some points and it has infringed the lower threshold (0 kN) in the fault condition.

The time base variations of 3-phase voltage of the primary windings are shown in Fig. 8. As seen in this figure, the voltages of phases "a" and "b" is increase about 8 times, when the primary enter the broken part. Worse still, their phase angles are same in this zone. As seen in this figure, the both of upper and lower threshold levels are broken by phases "a" and "b".

The various components of 3-phase voltages with HHT analysis is plotted in Fig. 9. As seen in this figure, the phases 1 and 2 have 5 IMFs, while the phase 3 has only 4 IMFs. In addition, the first and second IMFs are bigger than other IMFs, with maximum amplitude of 2 kV. However, its value before fault is 247 V. Moreover, the phase 2 is more affected by this fault and the all IMFs of this phase is higher than others.

The time–frequency analysis by HHS is presented in Fig. 10. In this figure, the faulted zone of all phases has lower frequency than healthy zone. In addition, the frequency of phase 2 is lower than others. It should be noted that the different values of frequency between 3-phase is due to their different angle. The energy of all phases in analyzed with power spectrum curve with signal analysis toolbox of Matlab software, which is shown in Fig. 11. As seen in this figure, the highest power is obtained by phase 2.

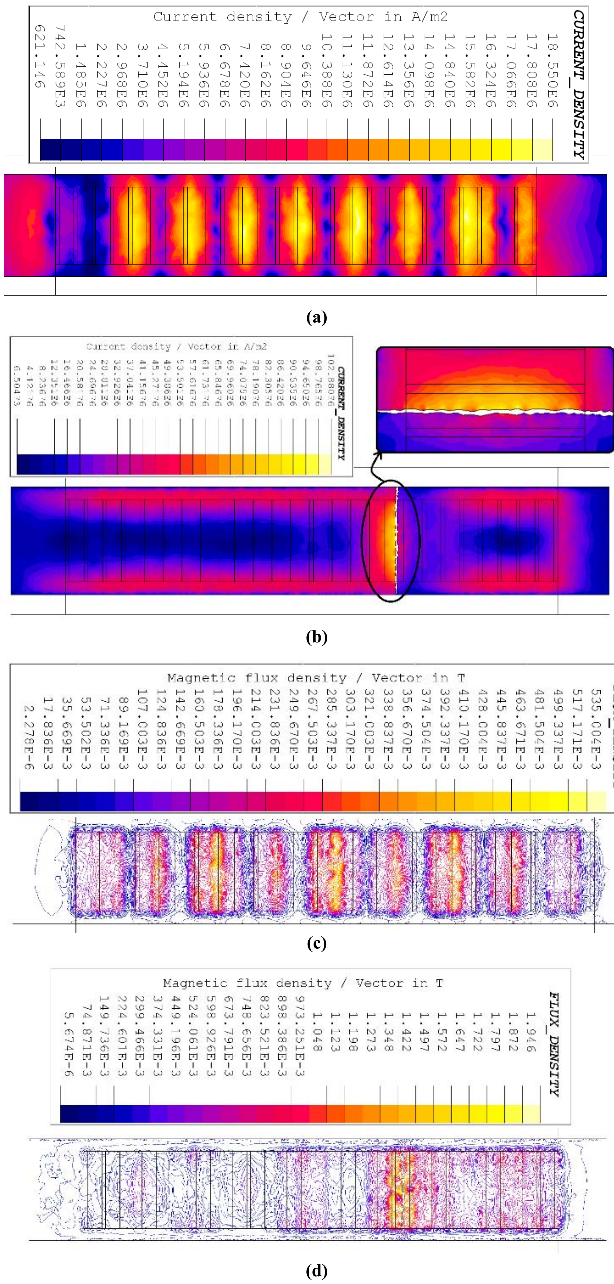

FIGURE 6. The distribution of current density and flux density in secondary sheet: a) current density in health sheet, b) current density in broken sheet, c) flux density in health sheet, d) flux density in broken sheet.

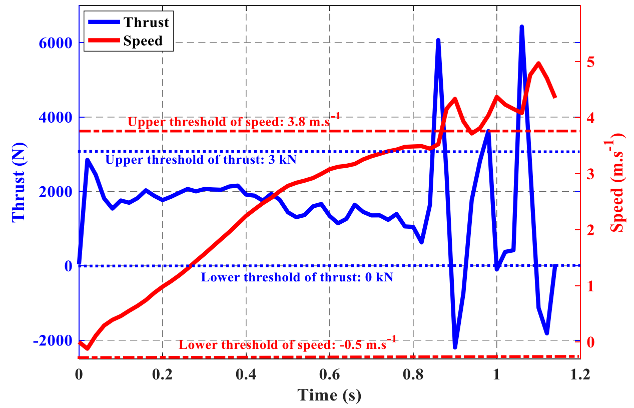

FIGURE 7. The variation of thrust and speed in various conditions.

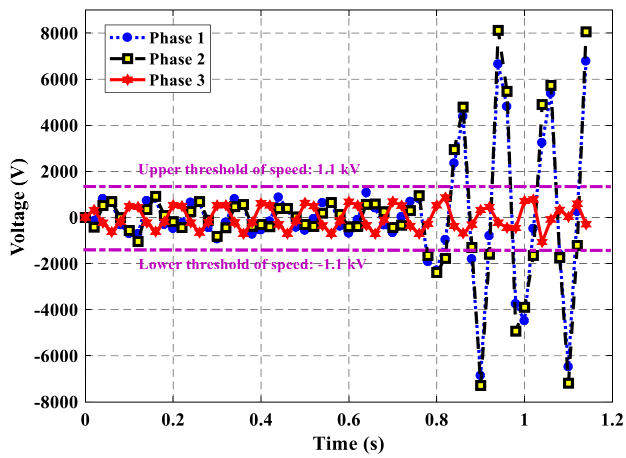

FIGURE 8. The variation of winding voltages under broken secondary.

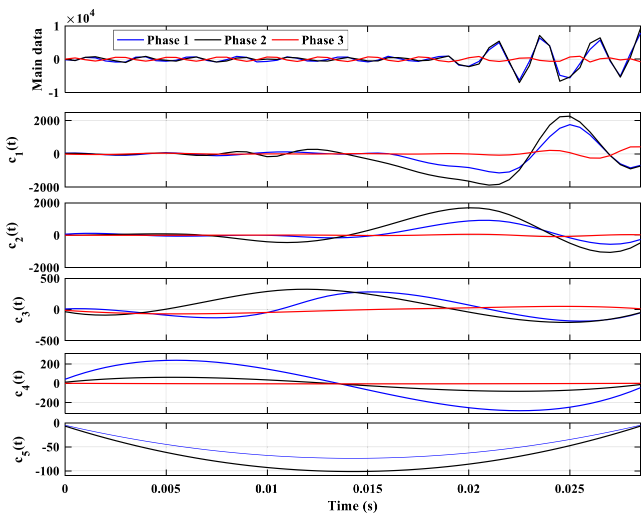

FIGURE 9. The HHT results of winding voltages under broken secondary.

2) THE INTER-TURN SHORT CIRCUIT IN PRIMARY WINDING

According to Fig. 5, each winding contains 4 coils that the simulated circuit in Flux software is shown in Fig. 12. As shown also in this figure, the second coil of phase b (Nb2) will be short circuit between interval time of [1.00, 1.40]. Moreover, the total simulation time is 1.50 s. The variations of speed and thrust is plotted in Fig. 13. The speed is reached to rated value, i.e. 3.5 m.s^{-1}, and the steady state value of thrust is 1 kN, before fault. The second level of threshold of speed in steady state is defined between 3.4 to 3.8 m.s^{-1}. Also, the second level of threshold of thrust in steady state is defined between 0.9 to 1.1 kN. In addition, the first threshold levels are defined as shown in Fig. 7. The speed and thrust of motor in the end of fault (at 1.4 s), both are decreased about 40%

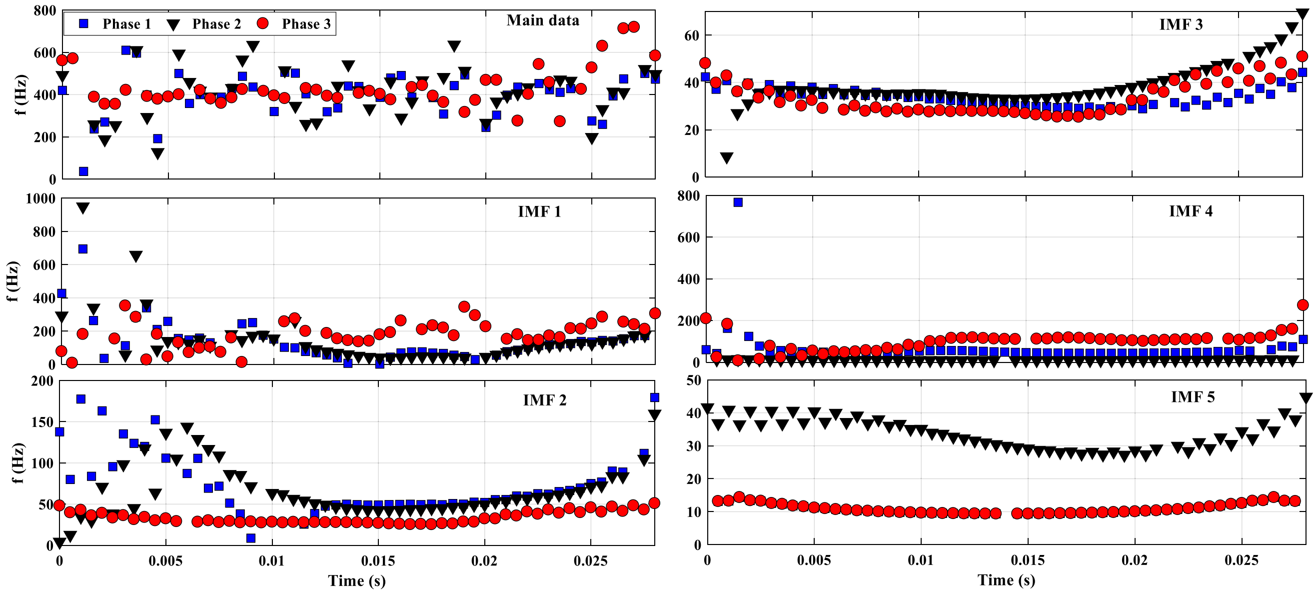

FIGURE 10. The HHS analysis of 3–phase voltages for various components in broken fault.

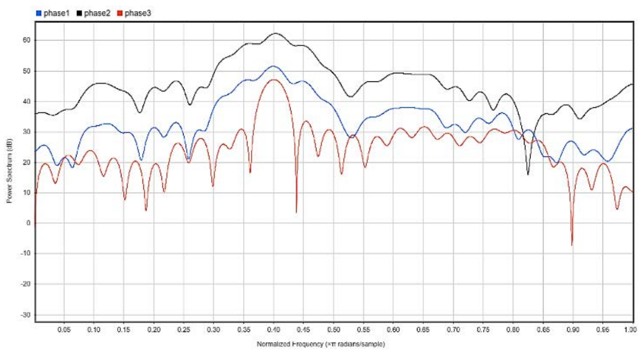

FIGURE 11. The power–spectrum analysis of 3-phase voltages in broken secondary.

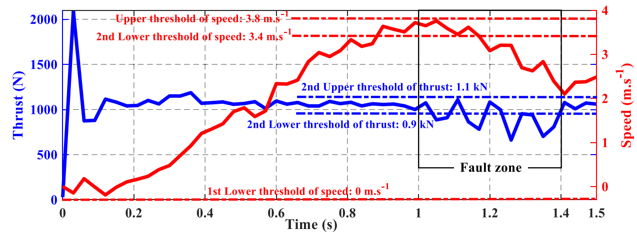

FIGURE 13. The variation of thrust and speed in various conditions (before fault, in short circuit, and after fault).

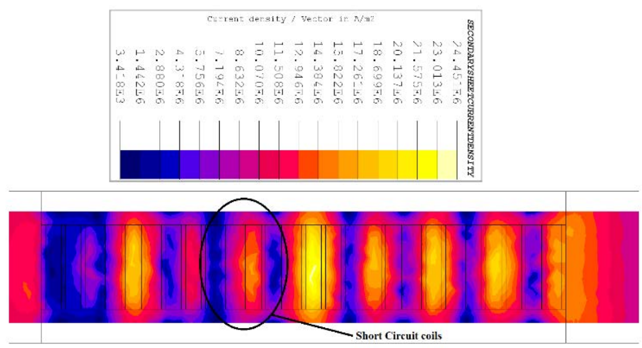

FIGURE 14. The distribution of current density in secondary sheet in short–circuit zone.

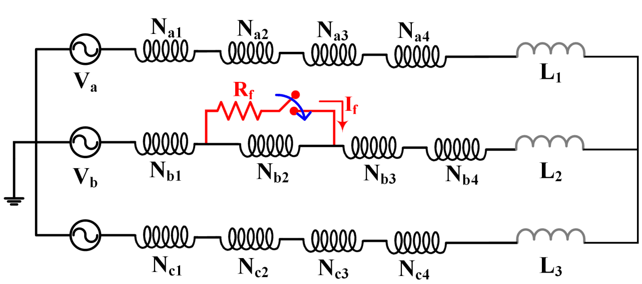

FIGURE 12. The simulated circuit of the HTS–SLIM.

and 35%, respectively. The distribution of current density is shown in Fig. 14, which the current density of region that is under the short– circuit coil is lower than others.

The current waveforms of all coils in phase "b" are shown in Fig. 15 (a). Moreover, the current variation of switch is shown in this figure. Due to low resistivity of HTS coils, the current of faulty coil is not zero and the sum of the currents of N_{b2} and switch is equal to the current of other coils. The HH analysis of healthy coils is shown in Fig. 15 (b) with considering $T = 1/F_s$, and $F_s = 2$ kHz in (48). As seen in this figure, the maximum amplitude is related to the first component, i.e. $c_1(t)$. The HH analysis of faulty coil is also

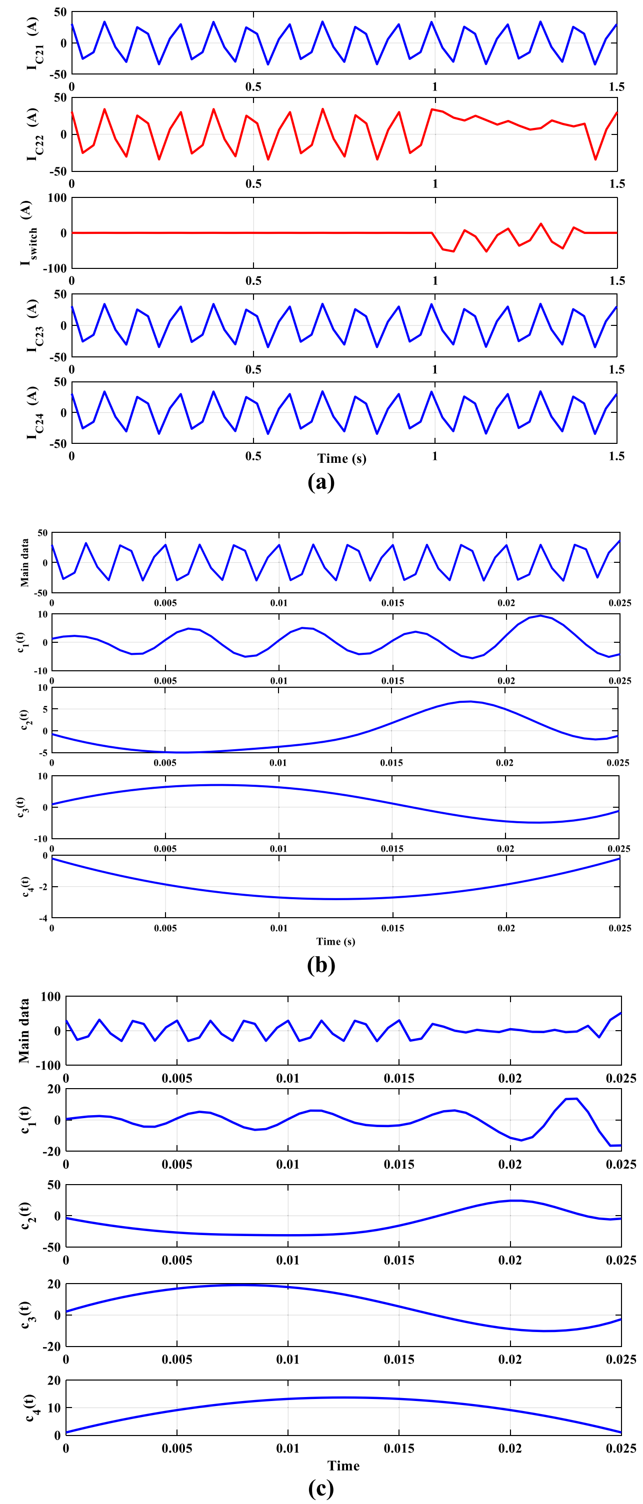

FIGURE 15. The current analysis of phase "b": a) the waveform of all coils and switch in terms of time, b) HHT result of current of health coils: Nb1, Nb3, and Nb4, c) HHT result of current of faulty coil: Nb2 distribution of current density in secondary sheet in short–circuit zone.

is shown in Fig. 15 (c). In this figure, the second component $c_2(t)$ has the maximum amplitude (± 50) and the first and the third components are oscillated between ± 20.

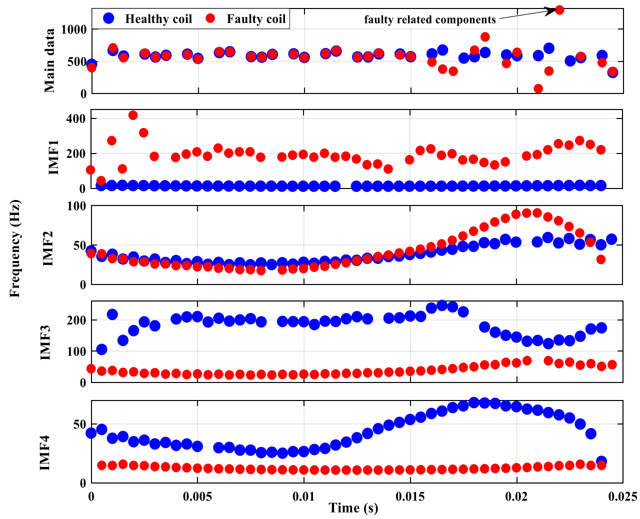

FIGURE 16. The HHS analysis of both faulty and healthy coils for various components.

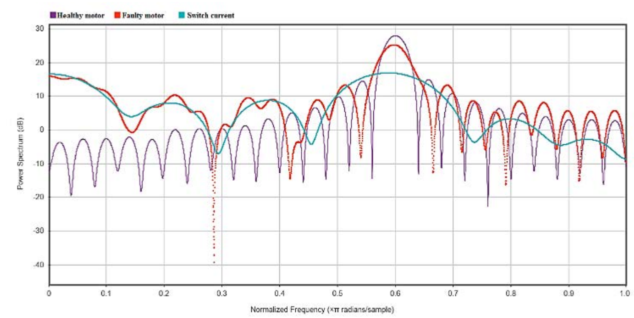

FIGURE 17. The power–spectrum analysis of of both faulty and healthy coils for various components.

The analysis of HHS is also done and the time–frequency planes of all components of IMFs ($n = 4$, see (47)) as well as main data, with both healthy and faulted coils, are plotted in Fig. 16. As seen in this figure, the main data of two coils has the maximum similarity before fault zone ($0.015 <$ time < 0.024). The maximum positive frequency of faulty coil in the main data is obtained as 1292 Hz, which show the lower current and higher energy.

The power–spectrum analysis of the current of healthy motor, faulty motor, and the short–circuit branch is carried out with signal analysis toolbox of Matlab software, and is shown in Fig. 17. As shown in this figure, the obtained power with short–circuit coil and switch is higher than healthy case.

V. DISCUSSION

The summarized results of the obtained data are rendered in Table 2. In the broken sheet fault, all parameters except of currents are increased, while they are decreased in short circuit fault. The maximum flux density of sheet under broken sheet fault is increased about 262 % that is so high. In addition, both of back–iron and primary core are saturated under this fault. Besides, the power loss of the secondary sheet is grew up that

TABLE 2. The various parameters variation under various faults.

Parameter	Broken sheet	Short–circuit	Simultaneously
B_{Max} in air gap	~ +122 %	~ –14 %	~ +101 %
B_{Max} in secondary sheet	~ +262 %	~ –35 %	~ +200 %
B_{Max} in back–Iron	~ +33 %	~ –34 %	~ –5 %
B_{Max} in primary core	~ +82 %	~ –5 %	~ +62 %
J_{Max} in secondary sheet	~ +543 %	~ –20 %	~ +511 %
Current of phase "a"	0 %	0 %	0 %
Current of phase "b"	0 %	–82 %	–80 %
Current of phase "c"	0 %	0 %	0 %
Back EMF of phase "a"	~ +725 %	0 %	~ +711 %
Back EMF of phase "b"	~ +800 %	~ –25 %	~ +759 %
Back EMF of phase "c"	~ +26 %	0 %	~ +18 %
Speed	~ +43 %	~ –42 %	~ +4 %
thrust	~ +600 %	~ –43 %	~ +560 %

causes increment of aluminum temperature. However, due to speed rising in this area, about 43 %, this temperature rising could be disregard, which is the SLIMs advantage, unless in applications that motor move back again. The thrust under broken sheet is also increased based on Table 2 and Fig. 7, which disrupts in the performance. The back EMFs of all windings are also increased, which is owing to increasing of speed.

In short–circuit fault, the speed and thrust are like decrement percentage, about −42 %. In addition, the back EMF of phase "b" is also decreased 25 %, due to only one coil of 4 coils is faulted. The maximum flux density of all components of motor under short circuit fault is reduced that are shown in Table 2. This Table could illustrate the main properties of each fault. This properties are also employed as a pattern in the next analysis. When this two faults are occurred simultaneously, the results could be combined together, based on Table 2.

Based on Table 2, the localization of fault could be carried out. In this method, the line (phase to phase) voltage is considered to detect the location of fault. The current and voltage of phase "b" under short circuit is non zero. Moreover, the back EMFs of 3-phase under broken sheet fault are increased that shows the mechanical fault. By considering the speed ($m.s^{-1}$) and start time of variation of it (s), the location (m) of fault could be found.

VI. CONCLUSION

In this paper, the dynamic model of the HTS–SLIM under both healthy and faulty modes is proposed and it was solved with FEM. In this proposed modeling, the end effects of SLIMs is considered for obtaining a comprehensive model. Moreover, the HHT is employed to detection the signal features of the voltages and currents for broken secondary and short–circuit primary, respectively. The results show that in broken secondary sheet, the voltages of windings could increase to about 8 times of its healthy condition. In addition, the thrust is also suddenly increased about 10 times. However, the increment rate of speed was about 25 %. The FEM results showed that the current density as well as flux density in the secondary conductor were increased at least 500 %. The short–circuit fault has vice versa results of broken case. In other words, the thrust and speed was decreased and the current density in aluminum sheet was reduced. With more assessment with HHT for detection the type of fault, it could be find out that broken secondary prepared lower harmonic frequencies and the short–circuit fault has introduced with higher ones. This result could be also obtained with power–spectrum analysis of the mentioned faults.

REFERENCES

[1] J. C. Trigeassou, *Electrical Machines Diagnosis*. Hoboken, NJ, USA: Wiley, 2013.

[2] A. G. Yetgin, "Effects of induction motor end ring faults on motor performance. Experimental results," *Eng. Failure Anal.*, vol. 96, pp. 374–383, Feb. 2019.

[3] M. B. Abd-el-Malek, A. K. Abdelsalam, and O. E. Hassan, "Novel approach using Hilbert Transform for multiple broken rotor bars fault location detection for three phase induction motor," *ISA trans.*, vol. 80, pp. 57–439, Sep. 2018.

[4] A. Glowacz, "Fault diagnosis of single-phase induction motor based on acoustic signals," *Mech. Syst. Signal Process.*, vol. 117, pp. 65–80, Feb. 2019.

[5] K. C. D. Kompella, V. G. R. Mannam, and S. R. Rayapudi, "DWT based bearing fault detection in induction motor using noise cancellation," *J. Electr. Syst. Inf. Technol.*, vol. 3, no. 3, pp. 411–427, Dec. 2016.

[6] G. Singh, T. C. Kumar, and V. N. Naikan, "Induction motor inter turn fault detection using infrared thermographic analysis," *Inf. Phys. Tech.*, vol. 77, pp. 82–277, Jul. 2016.

[7] T. Ameid, A. Menacer, H. Talhaoui, and Y. Azzoug, "Discrete wavelet transform and energy eigen value for rotor bars fault detection in variable speed field-oriented control of induction motor drive," *ISA Trans.*, vol. 79, pp. 217–231, Aug. 2018.

[8] M. Khanjani and M. Ezoji, "Electrical fault detection in three-phase induction motor using deep network-based features of thermograms," *Measurement*, vol. 173, Mar. 2021, Art. no. 108622.

[9] A. Namdar, H. Samet, M. Allahbakhshi, M. Tajdinian, and T. Ghanbari, "A robust stator inter-turn fault detection in induction motor utilizing Kalman filter-based algorithm," *Measurement*, vol. 187, Jan. 2022, Art. no. 110181.

[10] A. Glowacz, "Acoustic based fault diagnosis of three-phase induction motor," *Appl. Acoust.*, vol. 137, pp. 82–89, Aug. 2018.

[11] P. A. Delgado-Arredondo, D. Morinigo-Sotelo, R. A. Osornio-Rios, J. G. Avina-Cervantes, H. Rostro-Gonzalez, and R. de Jesus Romero-Troncoso, "Methodology for fault detection in induction motors via sound and vibration signals," *Mech. Syst. Signal Process.*, vol. 83, pp. 568–589, Jan. 2017.

[12] M. J. Duran, I. Gonzalez-Prieto, N. Rios-Garcia, and F. Barrero, "A simple, fast, and robust open-phase fault detection technique for six-phase induction motor drives," *IEEE Trans. Power Electron.*, vol. 33, no. 1, pp. 547–557, Jan. 2018.

[13] L. A. Trujillo-Guajardo, J. Rodriguez-Maldonado, M. A. Moonem, and M. A. Platas-Garza, "A multiresolution Taylor–Kalman approach for broken rotor bar detection in cage induction motors," *IEEE Trans. Instrum. Meas.*, vol. 67, no. 6, pp. 1317–1328, Jun. 2018.

[14] T. Yang, H. Pen, Z. Wan, and C. S. Chang, "Feature knowledge based fault detection of induction motors through the analysis of stator current data," *IEEE Trans. Instrum. Meas.*, vol. 65, no. 3, pp. 58–549, Jan. 2016.

[15] L. Frosini, C. Harlisca, and L. Szabo, "Induction machine bearing fault detection by means of statistical processing of the stray flux measurement," *IEEE Trans. Ind. Electron.*, vol. 62, no. 3, pp. 1846–1854, Mar. 2015.

[16] J. R. Rivera-Guillen, J. J. De Santiago-Perez, J. P. Amezquita-Sanchez, M. Valtierra-Rodriguez, and R. J. Romero-Troncoso, "Enhanced FFT-based method for incipient broken rotor bar detection in induction motors during the startup transient," *Measurement*, vol. 124, pp. 277–285, Aug. 2018.

[17] F. B. Batista, P. C. M. L. Filho, R. Pederiva, and V. A. D. Silva, ''An empirical demodulation for electrical fault detection in induction motors,'' *IEEE Trans. Instrum. Meas.*, vol. 65, no. 3, pp. 559–569, Mar. 2016.

[18] A. G. Espinosa, J. A. Rosero, J. Cusidó, L. Romeral, and J. A. Ortega, ''Fault detection by means of Hilbert–Huang transform of the stator current in a PMSM with demagnetization,'' *IEEE Trans. Energy Convers.*, vol. 25, no. 2, pp. 312–318, Jun. 2010.

[19] J. A. Antonino-Daviu, M. Riera-Guasp, M. Pineda-Sanchez, R. Puche-Panadero, R. B. Pérez, P. Jover-Rodriguez, and A. Arkkio, ''Fault diagnosis in induction motors using the Hilbert-huang transform,'' *Nucl. Technol.*, vol. 173, no. 1, pp. 26–34, Jan. 2011.

[20] F.-L. Niu, J. Huang, J.-Q. Yang, L.-Y. Chen, and H. Jin, ''Rotor broken-bar fault diagnosis of induction motor based on HHT of the startup electromagnetic torque,'' *Frontiers Electr. Electron. Eng. China*, vol. 1, no. 2, pp. 188–193, Jun. 2006.

[21] E. Elbouchikhi, V. Choqueuse, Y. Amirat, M. E. H. Benbouzid, and S. Turri, ''An efficient Hilbert–Huang transform-based bearing faults detection in induction machines,'' *IEEE Trans. Energy Convers.*, vol. 32, no. 2, pp. 401–413, Jun. 2017.

[22] J. F. Martins, V. F. Pires, and T. Amaral, ''Induction motor fault detection and diagnosis using a current state space pattern recognition,'' *Pattern Recognit. Lett.*, vol. 32, no. 2, pp. 321–328, Jan. 2011.

[23] R. Yan, R. X. Gao, and X. Chen, ''Wavelets for fault diagnosis of rotary machines: A review with applications,'' *Signal Proc.*, vol. 96, pp. 1–5, Mar. 2014.

[24] B. Bessam, A. Menacer, M. Boumehraz, and H. Cherif, ''DWT and Hilbert transform for broken rotor bar fault diagnosis in induction machine at low load,'' *Energy Proc.*, vol. 74, pp. 1248–1257, Aug. 2015.

[25] G. A. Jiménez, A. O. Muñoz, and M. A. Duarte-Mermoud, ''Fault detection in induction motors using Hilbert and wavelet transforms,'' *Electr. Eng.*, vol. 89, no. 3, pp. 205–220, Jan. 2007.

[26] C. Combastel, S. Lesecq, S. Petropol, and S. Gentil, ''Model-based and wavelet approaches to induction motor on-line fault detection,'' *Control Eng. Pract.*, vol. 10, no. 5, pp. 493–509, May 2002.

[27] I. Martin-Diaz, D. Morinigo-Sotelo, O. Duque-Perez, R. A. Osornio-Rios, and R. J. Romero-Troncoso, ''Hybrid algorithmic approach oriented to incipient rotor fault diagnosis on induction motors,'' *ISA Trans.*, vol. 80, pp. 427–438, Sep. 2018.

[28] M. F. S. V. D'Angelo, R. M. Palhares, R. H. C. Takahashi, R. H. Loschi, L. M. R. Baccarini, and W. M. Caminhas, ''Incipient fault detection in induction machine stator-winding using a fuzzy-Bayesian change point detection approach,'' *Appl. Soft Comput.*, vol. 11, no. 1, pp. 179–192, Jan. 2011.

[29] W. Sun, R. Zhao, R. Yan, S. Shao, and X. Chen, ''Convolutional discriminative feature learning for induction motor fault diagnosis,'' *IEEE Trans. Ind. Informat.*, vol. 13, no. 3, pp. 1350–1359, Jun. 2017.

[30] B. Bessam, A. Menacer, M. Boumehraz, and H. Cherif, ''Detection of broken rotor bar faults in induction motor at low load using neural network,'' *ISA Trans.*, vol. 64, pp. 241–246, Sep. 2016.

[31] H. Yaghobi, ''Stator turn-to-turn fault detection of induction motor by non-invasive method using generalized regression neural network,'' *Iran. J. Elec. Elec. Eng.*, vol. 13, nos. 177–188, Mar. 2017.

[32] X. Liang, M. Z. Ali, and H. Zhang, ''Induction motors fault diagnosis using finite element method: A review,'' *IEEE Trans. Ind. Appl.*, vol. 56, no. 2, pp. 1205–1217, Mar. 2020.

[33] R. Fiser and S. Ferkolj, ''Application of a finite element method to predict damaged induction motor performance,'' *IEEE Trans. Magn.*, vol. 37, no. 5, pp. 3635–3639, Sep. 2001.

[34] H. H. Eldeeb, A. Berzoy, and O. Mohammed, ''Stator fault detection on DTC-driven IM via magnetic signatures aided by 2-D FEA co-simulation,'' *IEEE Trans. Magn.*, vol. 55, no. 6, pp. 1–5, Jun. 2019.

[35] F. Immovilli, C. Bianchini, M. Cocconcelli, A. Bellini, and R. Rubini, ''Bearing fault model for induction motor with externally induced vibration,'' *IEEE Trans. Ind. Electron.*, vol. 60, no. 8, pp. 3408–3418, Aug. 2013.

[36] X. Ying, ''Performance evaluation and thermal fields analysis of induction motor with broken rotor bars located at different relative positions,'' *IEEE Trans. Mag.*, vol. 46, no. 5, pp. 1243–1250, Feb. 2010.

[37] J. Faiz, B. M. Ebrahimi, and H. A. Toliyat, ''Effect of magnetic saturation on static and mixed eccentricity fault diagnosis in induction motor,'' *IEEE Trans. Magn.*, vol. 45, no. 8, pp. 3137–3144, Aug. 2009.

[38] A. Bentounsi and A. Nicolas, ''On line diagnosis of defaults on squirrel cage motors using FEM,'' *IEEE Trans. Magn.*, vol. 34, no. 5, pp. 3511–3514, Sep. 1998.

[39] B. M. Ebrahimi, A. M. Takbash, and J. Faiz, ''Losses calculation in line-start and inverter-fed induction motors under broken bar fault,'' *IEEE Trans. Instrum. Meas.*, vol. 62, no. 1, pp. 140–152, Jan. 2013.

[40] A. Ordaz-Moreno, R. de Jesus Romero-Troncoso, J. A. Vite-Frias, J. R. Rivera-Gillen, and A. Garcia-Perez, ''Automatic online diagnosis algorithm for broken-bar detection on induction motors based on discrete wavelet transform for FPGA implementation,'' *IEEE Trans. Ind. Electron.*, vol. 55, no. 5, pp. 2193–2202, May 2008.

[41] J. F. Bangura and N. A. Demerdash, ''Effects of broken bars/end-ring connectors and airgap eccentricities on ohmic and core losses of induction motors in ASDs using a coupled finite element-state space method,'' *IEEE Trans. Energy Convers.*, vol. 15, no. 1, pp. 40–47, Mar. 2000.

[42] X. Ying, ''Characteristic performance analysis of squirrel cage induction motor with broken bars,'' *IEEE Trans. Mag.*, vol. 45, no. 2, pp. 759–766, Feb. 2009.

[43] Y. Gao, X. Liu, and J. Xiang, ''FEM simulation-based generative adversarial networks to detect bearing faults,'' *IEEE Trans. Ind. Informat.*, vol. 16, no. 7, pp. 4961–4971, Jul. 2020.

[44] G. Curcuru, M. Cocconcelli, F. Immovilli, and R. Rubini, ''On the detection of distributed roughness on ball bearings via stator current energy: Experimental results,'' *Diagnostyka*, vol. 3, no. 51, pp. 17–21, Aug. 2009.

[45] L. Frosini and E. Bassi, ''Stator current and motor efficiency as indicators for different types of bearing faults in induction motors,'' *IEEE Trans. Ind. Electron.*, vol. 57, no. 1, pp. 244–251, Jan. 2010.

[46] M. Malekpour, B. T. Phung, and E. Ambikairajah, ''Online technique for insulation assessment of induction motor stator windings under different load conditions,'' *IEEE Trans. Dielectr. Electr. Insul.*, vol. 24, no. 1, pp. 349–358, Feb. 2017.

[47] O. A. Mohammed, N. Y. Abed, and S. Ganu, ''Modeling and characterization of induction motor internal faults using finite-element and discrete wavelet transforms,'' *IEEE Trans. Magn.*, vol. 42, no. 10, pp. 3434–3436, Oct. 2006.

[48] N. Praveen Kumar and T. B. Isha, ''Application of empirical wavelet transform for analyzing inter-turn fault in FEM based closed loop speed controlled induction motor,'' in *Proc. IEEE Int. Conf. Power Electron., Drives Energy Syst. (PEDES)*, Dec. 2020, pp. 1–6.

[49] K. Prasob, N. P. Kumar, and T. B. Isha, ''Inter-turn short circuit fault analysis of PWM inverter fed three-phase induction motor using finite element method,'' in *Proc. Int. Conf. Circuit,Power Comput. Technol. (ICCPCT)*, Apr. 2017, pp. 1–6.

[50] K. Edomwandekhoe and X. Liang, ''Advanced feature selection for broken rotor bar faults in induction motors,'' in *Proc. IEEE/IAS 54th Ind. Commercial Power Syst. Tech. Conf. (I&CPS)*, May 2018, pp. 1–10.

[51] X. Liu, H. Huang, and J. Xiang, ''A personalized diagnosis method to detect faults in a bearing based on acceleration sensors and an FEM simulation driving support vector machine,'' *Sensors*, vol. 20, no. 2, pp. 1–13, Jan. 2020.

[52] A. Sapena-Bano, F. Chinesta, M. Pineda-Sanchez, J. V. Aguado, D. Borzacchiello, and R. Puche-Panadero, ''Induction machine model with finite element accuracy for condition monitoring running in real time using hardware in the loop system,'' *Int. J. Elect. Power Energy Syst.*, vol. 111, pp. 315–324, Oct. 2019.

[53] A. Berzoy, A. A. S. Mohamed, and O. Mohammed, ''Complex-vector model of interturn failure in induction machines for fault detection and identification,'' *IEEE Trans. Ind. Appl.*, vol. 53, no. 3, pp. 2667–2678, May 2017.

[54] A. Berzoy, A. A. S. Mohamed, and O. Mohammed, ''Impact of inter-turn short-circuit location on induction machines parameters through FE computations,'' *IEEE Trans. Magn.*, vol. 53, no. 6, pp. 1–4, Jun. 2017.

[55] R. M. Tallam, T. G. Habetler, and R. G. Harley, ''Transient model for induction machines with stator winding turn faults,'' *IEEE Trans. Ind. Appl.*, vol. 38, no. 3, pp. 632–637, May/Jun. 2002.

[56] N. E. Huang and S. S. P. Shen, *Hilbert-Huang Transform and its Applications*, vol. 16, 2nd ed. Chicago, IL, USA: World Scientific, 2013.

[57] A. Ahmadpour, A. Dejamkhooy, and H. Shayeghi, ''HTS–SLIM design based on Bayesian multi–level, multi–objective optimization and Gaussian process models,'' *Phys. C, Supercond. Appl.*, vol. 591, Dec. 2021, Art. no. 1353970.

ALI AHMADPOUR received the B.Sc. degree from Urmia University, Urmia, Iran, in 2014, and the M.Sc. degree from the University of Tabriz, Tabriz, Iran, in 2016. He is currently pursuing the Ph.D. degree with the University of Mohaghegh Ardabili, Ardabil, Iran. His research interests include design and control of electrical machines, linear motors, optimization methods, renewable energy, smart homes, and application of machine learning methods in electrical systems.

ABDOLMAJID DEJAMKHOOY was born in Ardabil, Iran, in 1983. He received the B.S. degree from the University of Tabriz, Tabriz, Iran, in 2006, and the M.S. and Ph.D. degrees in electrical engineering from the Shahrood University of Technology, Shahrood, Iran, in 2009 and 2014, respectively. He is currently with the Department of Electrical Engineering. University of Mohaghegh Ardabili, Ardabil, Iran. His research interests include optimal design of electrical machines, power system analysis, and processing of power system signals.

HOSSEIN SHAYEGHI (Senior Member, IEEE) received the Ph.D. degree in electrical engineering from the Iran University of Science and Technology, Tehran, Iran, in 2006. He is currently a Full Professor and the Scientific Director with the Energy Management Research Center, University of Mohaghegh Ardabili, Ardabil, Iran. He has authored or coauthored of 14 book chapters in international publishers and more than 430 articles in international journals and conference proceedings that received in Google Scholar more than 6000 citations with an H-index equal to 40. His research interests include power system control and operation, microgrid and smart grids control and energy management, and FACTs device. He has been included in the Thomson Reuter's list of the top 1% of most-cited technical engineering scientists, from 2015 to 2020, continuously. He is also the Editor-in-Chief of *Journal of Operation and Automation in Power Engineering* and *Journal of Energy Management and Technology*.